How to cite: *Angew. Chem. Int. Ed.* **2021**, *60*, 25958–25965
International Edition: doi.org/10.1002/anie.202110515
German Edition: doi.org/10.1002/ange.202110515

Metalloporphyrins Hot Paper

Room-Temperature Spin-Dependent Transport in Metalloporphyrin-Based Supramolecular Wires

Albert C. Aragonès, Alejandro Martín-Rodríguez, Daniel Aravena, Giuseppe di Palma, Wenjie Qian, Josep Puigmartí-Luis, Núria Aliaga-Alcalde, Arántzazu González-Campo, Ismael Díez-Pérez, and Eliseo Ruiz**

Abstract: *Here we present room-temperature spin-dependent charge transport measurements in single-molecule junctions made of metalloporphyrin-based supramolecular assemblies. They display large conductance switching for magnetoresistance in a single-molecule junction. The magnetoresistance depends acutely on the probed electron pathway through the supramolecular wire: those involving the metal center showed marked magnetoresistance effects as opposed to those exclusively involving the porphyrin ring which present nearly complete absence of spin-dependent charge transport. The molecular junction magnetoresistance is highly anisotropic, being observable when the magnetization of the ferromagnetic junction electrode is oriented along the main molecular junction axis, and almost suppressed when it is perpendicular. The key ingredients for the above effect to manifest are the electronic structure of the paramagnetic metalloporphyrin, and the spinterface created at the molecule–electrode contact.*

Introduction

Magnetoresistance is the crucial property in a spintronic device.[1,2] It is well-understood in devices composed by multilayered inorganic materials; usually a non-magnetic layer sandwiched between two ferromagnetic electrodes[3–5] Molecular systems are an appealing alternative because they offer large tunability via chemical modifications.[6–10] Molecular-based spintronic devices mostly exploit single-molecule magnets (e.g. phtalocyaninato Tb^{III}), which must be employed at cryogenic temperatures to preserve their intrinsic molecular magnetic properties, thus severely limiting technological applications.[11–14] Few types of molecular spintronic devices have been recently described displaying room temperature spin-dependent transport: (i) chiral diamagnetic molecules, such as DNA and peptides, displaying chiral induced spin selectivity (CISS) in a variety of different device configurations,[15–19] (ii) single-molecule junctions using spin-crossover molecules based on triazole-pyridine transition metal complexes $[M(tzpy)_2(NCX)_2]$, (M: Fe or Co; X: S or Se) in their high-spin configuration,[20,21] and (iii) single-molecule junctions of the form Fe-terephthalic acid-Fe under a magnetic field.[22] Interestingly, cases (i-ii) are performed in the absence of a magnetic field; the molecular structures are bridged between a dielectric metal electrode (typically a noble metal such as Au or Pt) and an ex situ magnetized ferromagnetic metal electrode (e.g. Ni or Co), and the inversion of the ferromagnet magnetization causes a large change in the conductance value through the molecular junction. In (ii), the observed exceedingly large spin-dependent effects can be explained by a subtle interplay between the electronic structure of the paramagnetic molecule and the metal substrate bearing large spin-orbit effects, which results in an effective spinterface.[1,23,24]

Here, we design, synthetize and characterize single-molecule spin-dependent transport of a series of metallopor-

[*] A. Martín-Rodríguez, E. Ruiz
Departament de Química Inorgànica i Orgànica
Diagonal 645, 08028 Barcelona (Spain)
E-mail: eliseo.ruiz@qi.ub.edu

A. C. Aragonès, I. Díez-Pérez
Department of Chemistry, Faculty of Natural & Mathematical Sciences, King's College London
Britannia House, 7 Trinity Street, London SE1 1DB (United Kingdom)
E-mail: ismael.diez_perez@kcl.ac.uk

A. Martín-Rodríguez, J. Puigmartí-Luis, E. Ruiz
Institut de Química Teòrica i Computacional
Universitat de Barcelona, Diagonal 645, 08028 Barcelona (Spain)

D. Aravena
Departamento de Química de los Materiales, Facultad de Química y Biología, Universidad de Santiago de Chile (USACH)
Casilla 40, Correo 33 (Chile)

G. di Palma, W. Qian, N. Aliaga-Alcalde, A. González-Campo
Institut de Ciència de Materials de Barcelona
ICMAB-CSIC, Campus UAB
08193 Bellaterra (Spain)

J. Puigmartí-Luis, N. Aliaga-Alcalde
ICREA (Institució Catalana de Recerca i Estudis Avançats)
Passeig Lluis Companys 23, 08010 Barcelona (Spain)

J. Puigmartí-Luis
Departament de Ciència dels Materials i Química Física
Diagonal 645, 08028 Barcelona (Spain)

A. C. Aragonès
Current address: Molecular Spectroscopy Department
Max Planck Institute for Polymer Research
Ackermannweg 10, 55128 Mainz (Germany)

Supporting information and the ORCID identification number(s) for the author(s) of this article can be found under: https://doi.org/10.1002/anie.202110515.

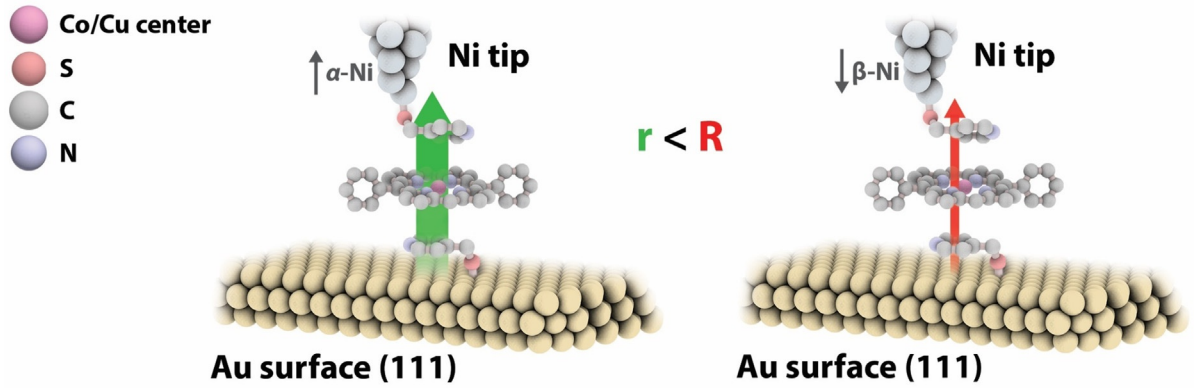

Figure 1. Representation of the studied magnetoresistance of the [Cu/Co(DPP)] systems showing a π–π supramolecular single-molecule junction under both Ni tip electrode magnetizations (labelled in the Figure as α-Ni and β-Ni).

phyrin with M^{II} (M: Co, Ni, Cu and Zn) and a 5,15-diphenylporphyrin (DPP) ligand.[25] The metalloporphyrin is supramolecularly trapped in a nanoscale gap by functionalizing both junction electrodes with pyridine-4-yl-methanethiol (PyrMT) coordinating ligands in a magnetically modified version of a scanning tunneling microscope (STM) break-junction system (Figure 1)[20,21] using both dynamic or *tapping* (monitoring the induced pulling of the molecular junction)[26,27] and static or *blinking* (monitoring the spontaneous molecular junction formation)[26,28] working modes. Our results reveal several new charge transport properties in a single-molecule junction: (i) among the different identified supramolecularly generated electron pathways through these molecular junctions,[29] the spin-dependent transport is exclusively observed in those where metal orbitals are directly participating in the junction formation. (ii) The observed spin-dependent transport is not limited to one direction of the current through the molecular junction (typically from the spin-polarized electrode to the diamagnetic metal electrode), but also observed in the opposite direction of the current flow between both junction electrodes. (iii) The direction of magnetization of the ferromagnetic electrode with respect to the charge transport direction is key for the manifestation of magnetoresistance, being more pronounced when the magnetization of the ferromagnetic electrode is parallel or antiparallel to the main molecular junction axis.

Results and Discussion

Single-molecule conductance experiments were first performed using a spin-polarized version of the STM break-junction approach (see details in Supplementary Information (SI) 1 and 2 sections).[20,21] Briefly, a freshly mechanically cut Ni tip was magnetically polarized ex situ by placing it within few millimeters proximity to a 1 T NdFeB magnet for a period of 2 h in an anaerobic chamber to preserve the tip from oxidation.[20] The magnitude of the Ni tip magnetization was characterized before and after the STM break-junction experiment using SQUID magnetometry to ensure that the Ni magnetization persisted over the entire time frame of the experiments (see SI section 3). After magnetization, both Ni tip and Au surface were functionalized with a pyridine-4-yl-methanethiol (PyrMT) under anaerobic and dark conditions (see SI section S4). The final exposed pyridine moiety in both electrodes' surfaces serves as the supramolecular ligands for the [M^{II}(DPP)] complexation (trapping) within the nanoscale junction yielding a PyrMT/[M^{II}(DPP)]/PyrMT junction arrangement (simplified as the [M(DPP)]/PyrMT assembly). The Ni tip was placed in the STM tip holder, the STM current feedback was turned off and the magnetized Ni tip was repeatedly driven in and out of contact to and from the Au(111) surface in successive cycles, using a 2-point feedback loop in the tunneling current flowing between the two STM tip and surface electrodes under a constant bias voltage. During the retraction stage, individual metalloporphyrins get trapped between the two functionalized electrodes as a result of the [M^{II}(DPP)]/PyrMT chemical interaction, yielding plateau-like features in the current versus retraction distance traces corresponding to the quantum conductance of the final single-molecule bridge. The percentage of individual traces displaying plateaus were typically 15–20 % of the total collected traces[22,30] (ca. 5000, see representative current captures in Figure 2 A) per experiment, which are then extracted out using automated algorithms and accumulated into the same conductance histogram (see the rejected curves in the SI section 1.5).

Figure 2 shows the three conductance features (high I, medium II and low III) previously characterized for this system corresponding to different supramolecular junction configurations as the interelectrode distance is increased.[29] Alpha/Beta labeled curves shows individual traces under opposite Ni electrode magnetizations along the main molecular junction axis. 1D semi-log histograms were then built out of several hundreds of current decay traces displaying current plateaus for each [M(DPP)]/PyrMT complex (see SI sections 1 and 4 for control experiments and additional methodological details, respectively). We used a negative sample bias meaning the injection of electrons goes from the non-magnetized Au substrate to the magnetized Ni tip that will act as the magnetoresistive electrons' drain. Similar results are obtained for the opposite bias voltage (see S1.6). The

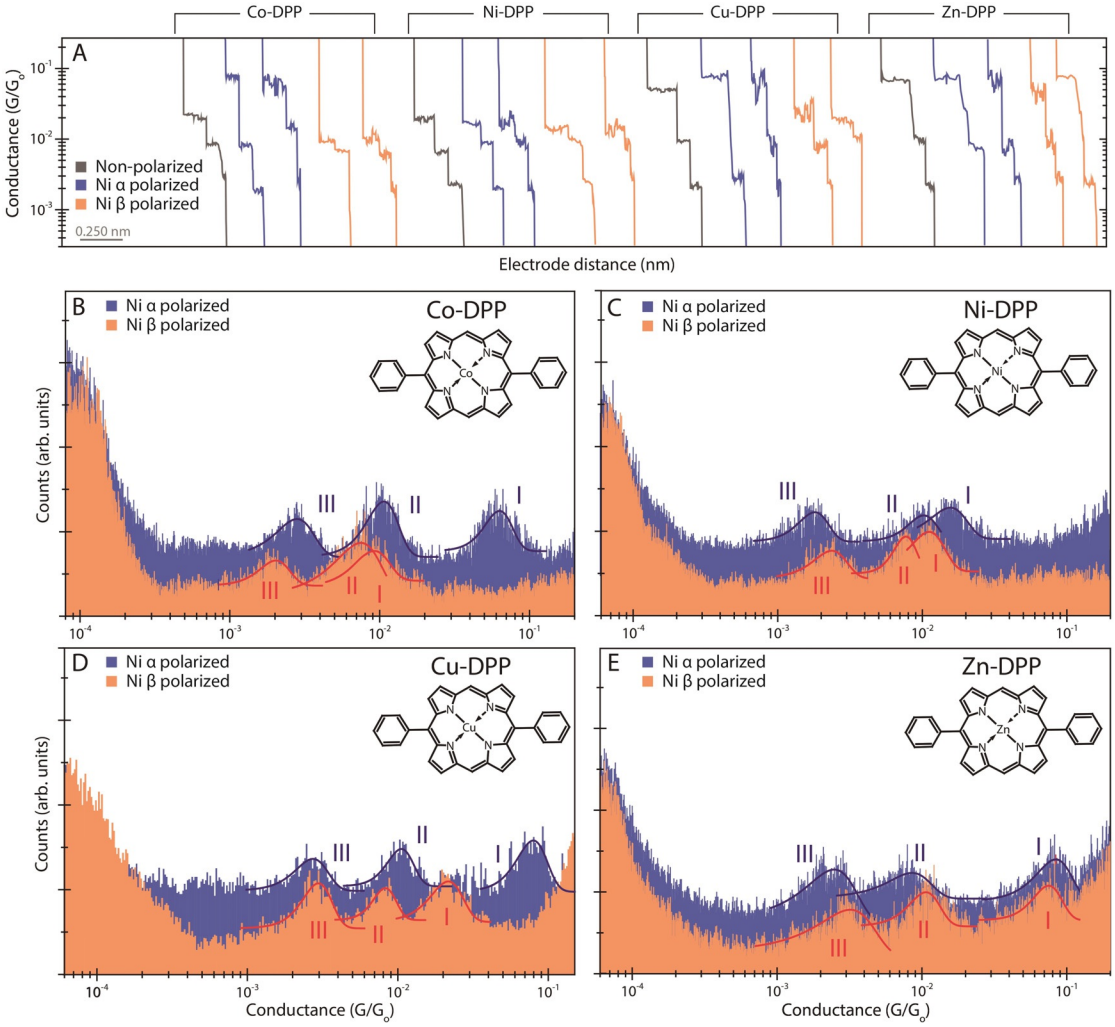

Figure 2. A) Representative individual current traces displaying plateau features used to build the 1D histograms in B–E. B–E) Single-molecule conductance 1D semi-log histograms for the metal porphyrins (labelled and represented in the Figure) bridging between Au and both α (blue) and β (orange) magnetically polarized Ni tips using PyrMT as anchoring ligand. Electrons are injected from the Au substrate to the Ni tip. All conductance values have been extracted from Gaussian fits of the peaks. Counts have been normalized versus the total amount of traces. All histograms display three peaks named conductance features I, II and III. The applied bias was set to −7.5 mV (see equivalent figures for positive bias in Figure S1.6).

conductance histograms were collected for both opposite magnetization signs of the Ni electrode along the main junction axis (α: up, β: down in Figure 2).

The three previously reported conductance features I-III for the [Co^{II}(DPP)]/PyrMT system,[29] are also identified in all four studied metal porphyrins (Co, Ni, Cu, Zn). In all cases, the low conductance features II and III display small variations upon inversion of the Ni tip magnetization direction, within narrow conductance ranges of 0.8–1 × 10^{-2} G_o and 2–3 × 10^{-3} G_o for II and III, respectively. These two conductance features have been previously ascribed to junction configurations arising from direct pyridinyl/DPP ring interactions via π–π stacking or/and hydrogen bonding with little or no orbital contribution from the metal center.[29] Likewise, the high conductance feature I has been univocally assigned to the pyridinyl coordination of the metal center[20] and it is observed that its conductance value depends on both the metal center (M^{II} = Co, Ni, Cu and Zn) and the Ni magnetization sign (α, β) (Figure 2). This observed magnetoresistance in the conductance feature I seems to be associated to the paramagnetic character of the metalloporphyrin.

The Co^{II} and Cu^{II} metalloporphyrin complexes, both paramagnetic systems, show a feature I conductance increasing under α-Ni tip magnetization and decreasing under β-Ni tip magnetization, being up to ca. 6-fold and 4-fold conductance difference for the [Co^{II}(DPP)], and [Cu^{II}(DPP)], respectively (Figure 3 A). It is worth noting that such conductance values are the largest reported for molecular system showing magnetoresistance effects.[21,22,31,32] Both [Co^{II}(DPP)]/PyrMT and [Cu^{II}(DPP)]/PyrMT observed magnetoresistance effect in the configuration I are also observed when the electrons are injected from the magnetic tip under reverse bias. In the latter, the conductance ratio against the inversion of the magnetization of the Ni tip is approximately 3-fold and 2-fold for [Co^{II}(DPP)]/PyrMT and [Cu^{II}(DPP)]/PyrMT, respectively (Figure 3 B).

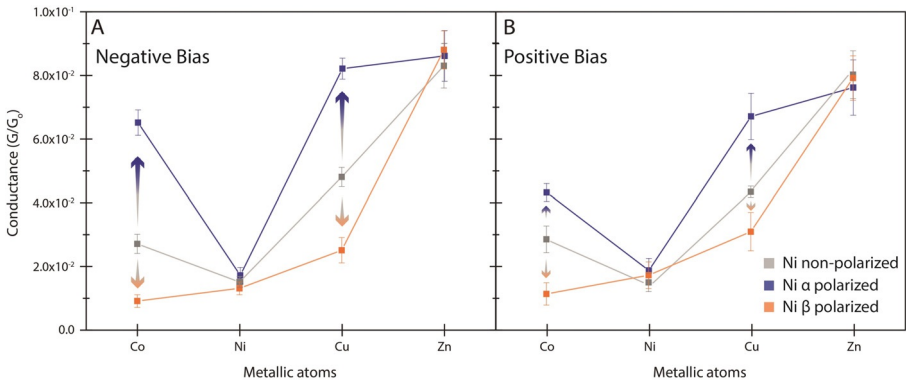

Figure 3. Graphs representing the high conductance feature I (A and B positive and negative bias, respectively) for each [M(DPP)]/PyrMT (indicated in the Figure) under non-magnetized, α and β magnetized Ni tips, represented in grey, blue and orange, respectively. Error bars denote the standard deviation of the Gaussian fits of the peaks shown in the histograms of Figures 2 and S.1.6.

Contrarily, the Ni^{II} and Zn^{II} systems do not show significant conductance dependence in the high conductance feature I under opposite magnetic polarizations of the Ni electrode (Figure 3). In the Zn^{II} case, the diamagnetism of the metalloporphyrin is the most straightforward explanation for these observations. It is surprising that the conductance feature I for the [Zn(DPP)]/PyrMT system scores the highest conductance value considering the closed d shell in its electronic structure. Equivalent experiments in the absence of PyrMT-tip functionalization (see SI section S1.3) reveal that no effective tip electrode/metalloporphyrin interactions are observed for the Co^{II}, Ni^{II} and Cu^{II} systems, while for the Zn^{II} one, a high conductance feature I of similar value to that found with the functionalized tip is obtained. This observation suggests that the preferable pentacoordination of the Zn^{II} center[33] might be preserved in the molecular junction, and that the top electrical contact is then established via direct contact with the metal STM probe surface, thus reducing the length of the transport channel and leading to a larger conductance value. Anomalously, the [Ni(DPP)]/PyrMT case does not show magnetoresistance (Figure 3), despite the Ni^{II} system being paramagnetic when adopting a hexacoordinated structure. Detailed DFT calculations (S5 section) show a small energy difference between $S=1$ high spin and $S=0$ low spin states when in the PyrMT/[Ni^{II}(DPP)]/PyrMT tunneling junction. Figure 3 also shows that the high conductance feature I for the [Ni(DPP)]/PyrMT and [Zn(DPP)]/PyrMT systems are identical to the ones in the experiments performed under non-magnetized Ni tip electrode (SI sections S1.1 and S1.2), while the [Co(DPP)]/PyrMT and [Cu(DPP)]/PyrMT under non-magnetization conditions yield an intermediate value between the ones obtained under α- and β-Ni tip polarizations.

To rule out possible structural disruption of the supramolecular adduct in the junction during the dynamic pulling, we studied the same magnetoresistance effects using a static STM junction approach based on the spontaneous formation of molecular bridges in a fixed tunneling gap (*blinking* mode, SI section 2).[26] Besides the more limited statistical information as compare to its *dynamic* counterpart, the static approach directly measures the conductance of the stochastically formed molecular bridge, avoiding disruptive mechanical pulling to get the conductance of the molecular junction, and also bringing information about the lifetime[34] (junction stability) of each distinct electrode/molecule interactions.[26,28,35] Briefly, this mode is based on recording current versus time transients at a fixed electrode-electrode distance when the feedback loop is disconnected.[28] When a molecular junction between the functionalized electrodes is stablished due to the [M^{II}(DPP)] trapping, the current suddenly jumps ("blinks") and lasts for a short period of time at room-temperature. Blink's timescale ranges between few tens to several hundred milliseconds depending on the anchoring groups and the intrinsic mechanical stability of the equipment. Even longer lifetimes can be observed using more stable molecule-electrode contact chemistry.[36–38] After that, the current abruptly drops to the initial tunneling value due to the spontaneous breakdown of the junction. The formation of mechanically stable molecular junctions is confirmed through an induced STM tip vertical pulling during the blinking lifetime and a subsequent analysis of the current decay trace. The appearance of current plateaus during the pulling trace collected during the blinking time evidences the stretching of the single-molecule bridge informing the blink was a consequence of an effective molecular junction formation.[26,36] Few hundreds of such blinks are set to the same time zero origin, background subtracted and accumulated into a 2D conductance maps without any data selection (SI section S4 for more details).

Blinking experiments were performed using a short electrode distance gap by imposing an initial set-point value of 7 nA allowing the [M^{II}(DPP)] molecules to be axially coordinated. The related experimental interelectrode distance was estimated to be between 1 to 1.5 nm considering coherent electron tunneling through the empty gap in the absence of a molecular bridge, which concur with the π-π stacked DFT optimized supramolecular structures spanning 0.9 to 1.1 nm in length (Figure 1).[29] Figures 4 a–c show the 2D conductance maps for the [Cu^{II}(DPP)] system under opposite magnetic magnetizations of the Ni tip (see also static single-molecule charge transport for all the other metals under non-magnetized conditions in the S2.2 section). The magnetoresistance effects observed in previous section are reproduced using the static mode, that is, invariability in the conductance features II and III under both Ni magnetization directions, and ca. 4-fold conductance difference in the high conductance feature I between α- and β-Ni magnetization directions. As previously reported, we also observe a similar trend for all metal systems in the junction stability; I > II > III.[25,39]

To expand the study over the anisotropy of the observed magnetoresistance effect in these systems, Figure 4 D shows a 2D conductance map performed applying a Ni tip magnet-

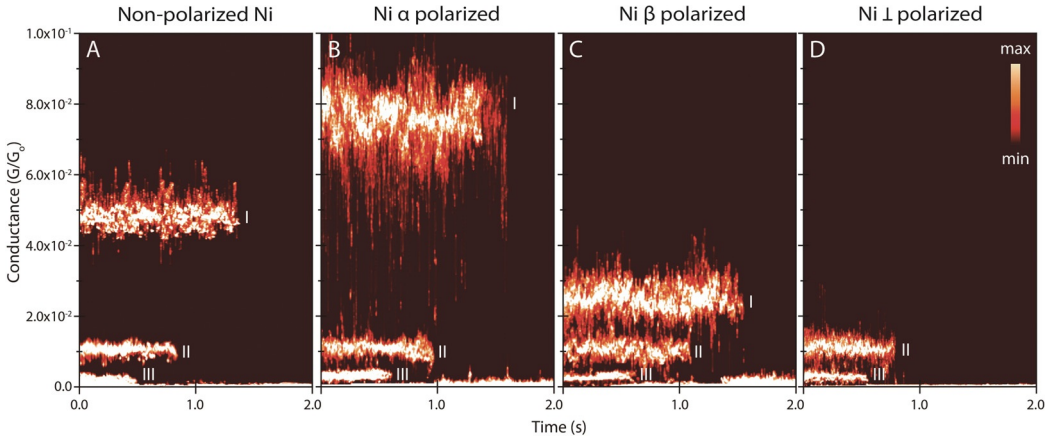

Figure 4. 2D conductance maps were obtained by accumulating hundreds of background-subtracted blinks set at a common time origin for [Cu(DPP)] under A) non-polarized, B) α-Ni tip, C) β-Ni-tip and D) perpendicularly magnetized electrodes. The 2D maps color counts were normalized versus the total number of counts. Applied voltage bias and initial setpoint currents were −7.5 mV and 7 nA, respectively.

ization oriented orthogonal to the main junction axis (named Ni ⊥). As in Figures 4 A–C, the magnetized Ni ⊥ has an effect on the high conductance feature I only, which is now not visible in the 2D plot suggesting that the measured conductance value falls below the detection limit of our current amplifier ($< 10^{-6}$ G$_o$). The latter evidences the strong anisotropy of the spin-dependent transport in these junctions with the direction of the tip magnetization.[22]

To rationalize the origin of the observed differences in transport properties in the studied single-molecule junctions, we performed periodic DFT calculations (see details in the SI section 5). The structural models for the calculations consisted in two true semi-infinite Au surface electrodes with the linker PyrMT molecule attached to both Au(111) surface via the thiol S atoms in a three-fold hollow configuration. The calculations were carried out using two equivalent Au surfaces and considering that the observed spin-filter effects arise from the mixing of the Au surface levels with the spin-polarized molecular orbitals in the paramagnetic metal center.[20,21,23,24] The Ni tip is not included in the calculation since it just controls the final device conductance because the transport of minority spin carriers is more efficient in the magnetically polarized Ni electrode.[40] After the initial supramolecular complex structure is optimized, we calculate the energy-dependent density of states (DOS) of the entire chemical adduct and evaluate the transmission function. From the calculated transmission at the Fermi level, the conductance G is theoretically extracted (see Computational details, SI section S5).

We started analyzing the conductance feature I–III for all M centres assuming a quasi-octahedral coordination in the [M^{II}(DPP)] with the two axially complexed nitrogen atoms of the PyrMT ligand in a "stacking" configuration (Figure 5 A–C right panels) as resulted from the DFT structure optimization.[29] Such structures yielded theoretical conductance values in very good agreement with the experimental ones (Figure 5 A–C, graphs green dots). Feature I conductance was also evaluated for other plausible supramolecular arrangements, namely, a fully orthogonal axial hexacoordination with two PyrMT axial ligand and a pure pentacoordination with just one PyrMT axial ligand (Figure 5 A blue and red dots, respectively). The latter configurations result both in conductance values of several orders of magnitude below the experimental ones, which were unexpectedly different considering the addition of PBE + U corrections in our calculations (see Methods Section). They were therefore not considered further for this study.

The calculated DOS and transmission curves for the two [M(DPP)]/PyrMT systems showing magnetoresistance (M = Co and Cu) are plotted in Figure 6 (see SI section S5.2 for the other two metals and lower conductance features II and III, and SI section S5.3 for equivalent results with hybrid functionals and non-periodic models). The main observed differences between the two studied metal systems are: (i) the Co^{II} system has a $S = 1/2$ electronic configuration $\left(d^2_{xy} d^2_{xz} d^2_{yz} d^1_{z^2} d^0_{x^2-y^2}\right)$. While the states closer to the Fermi level are originated in the porphyrin ring (Figure 6 A), we do observe metal contribution to transport appearing relatively close in energy to the Fermi level as the highest occupied beta d_{xz} and d_{yz} orbitals. (ii) The Cu^{II} case also has a $S = 1/2$ electronic configuration $\left(d^2_{xy} d^2_{xz} d^2_{yz} d^2_{z^2} d^1_{x^2-y^2}\right)$. Similarly, the orbitals closer to the Fermi level are those of the porphyrin ring, with empty $d_{x^2-y^2}$ metal orbital (Figure 6 B) relatively close in energy to the Fermi level. However, the $d_{x^2-y^2}$ orbital is perpendicular to the transmission pathway, resulting in the observed narrow peak (Figure 6 B) in the transmission due to the weak interaction between this molecular orbital and the electrode levels. The experimental magnetoresistance observed in the conductance feature I for both [Co(DPP)]/PyrMT and [Cu(DPP)]/PyrMT systems points to the involvement of metal-based spin-polarized orbitals in the main transport pathways. According to the PDOS from both periodic and discrete calculations (Figure 6 and SI sections S5.2 and S5.3), the closest orbitals (ca. 0.2 eV below) to the electrodes Fermi levels correspond to non spin-polarized ligand orbitals, while occupied metal orbitals appear at larger 0.5–1 eV energies from the Fermi level.

While the molecular orbital energies give a general picture of the available molecular states for electron transport, the spin-polarization found at DFT-NEGF is too small

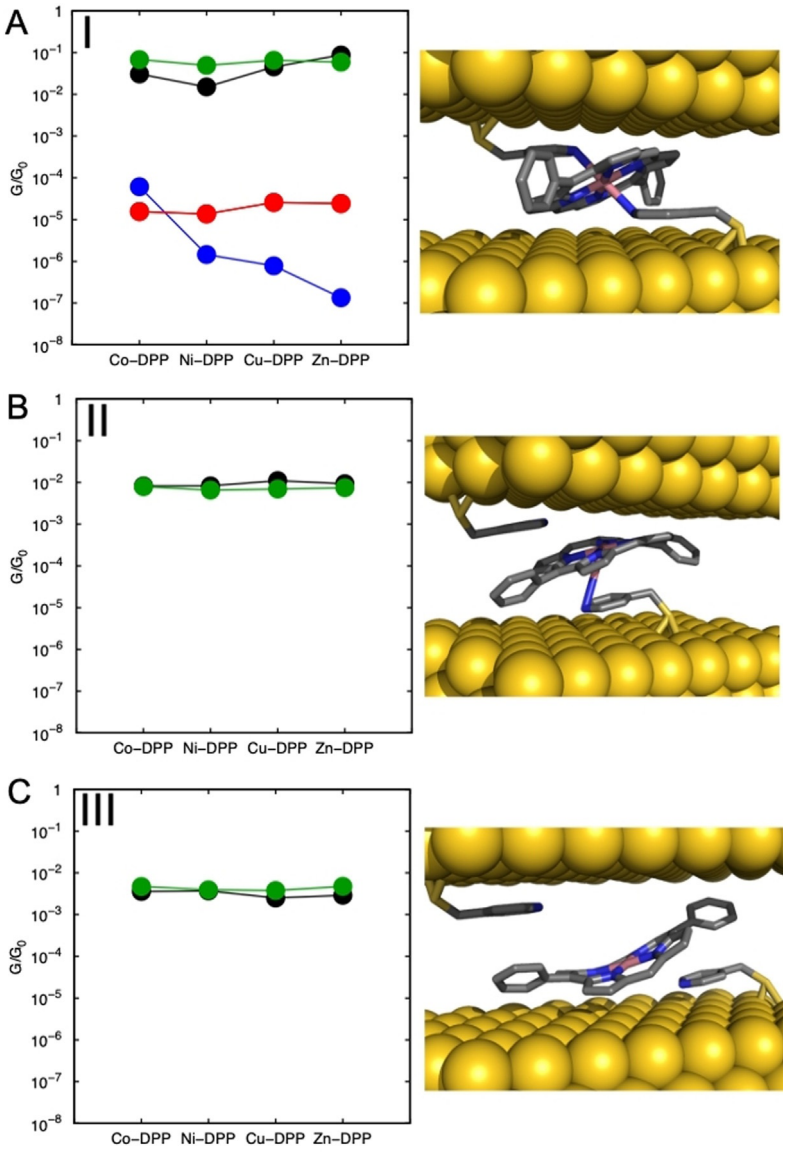

Figure 5. Graphs (left column in A–C) representing the experimental (black dots) and DFT calculated conductance values (green, red, blue dots) for the three single-molecule junction conductance signatures I–III (see zoom-in more detailed graph in Figure S5.1). The values for the high conductance feature I in (A) were calculated using DFT optimized stacking structures illustrated in the right panel for the Co^{II} system case (green dots), using an optimized hexacoordinated model with two axial thiol-pyridine PyrMT ligands (blue dots) and using a pentacoordinated model with one axial ligand only (red dots).

to justify the experimental results. It should be kept in mind that DFT-NEGF assumes a non-interacting nature of the electrons including partially non-equilibrium effects. However, it employs an equilibrium description using ground state of the molecule only to analyze a non-equilibrium property, namely, charge transport in a molecular junction.[41] Thus, an alternative is to complete such theoretical study by using time dependent DFT (TD-DFT) calculations to check the nature of the possible excited stated involved in the transport process.

To understand the nature of the observed magnetoresistance effects in both Co- and Cu-based single-molecule junctions, we expand the ground state transmission picture in Figure 6 to the analysis of the spin-polarized nature of molecular excited states involved in the transport process. To compare both types of transport channels, we must go beyond the orbital energy gap, since such approximation misses key dynamic effects of the charge transport process in a molecular junction, where the system evolves temporally resulting in a mixture of excited states with the ground state. Thus, a steady state picture is not enough to describe all the effects associated to the transport process as stated above.[42] To capture such dynamics, we employ TD-DFT (see SI section S5) to approximately account for the energy states associated with neutral excitations.[43] Figure 7 summarizes the TD-DFT results highlighting the participation of the metal centers in the lowest energy transitions, which are key for the low bias conductance of the system. This finding contrasts with the DFT-NEGF orbital energy ordering, where HOMO and LUMO frontier orbitals involved in the charge transport process were ligand centered. In both cases, low energy excitations involve mixtures of ligand (porphyrin rings) and metal-based orbitals. As expected, ligand-related transitions are not spin polarized as observed by equidistance blue (spin down) and red (spin up) vertical bars (Figure 7), while excitations involving metal orbitals show a dominant spin orientation. [Cu(DPP)] shows three spin-polarized low energy transitions which are mostly of beta character (Figure 7B, blue bars between 850 and 1200 nm), associated with the empty $d_{x^2-y^2}$ orbital. In the [Co(DPP)] case, the spin polarization in the current can then arise as the result of a subtle balance of spin channels, some of them with majority alpha contribution (Figure 7A three bars at 1000 and above 1400 nm) and beta (two bars close to 900 nm). This picture differs from the behavior found previously for much larger magnetoresistance effects reported in single-molecule junctions composed of $[M(tzpy)_2(NCX)_2]$ complexes (M = Fe and Co, X = S and Se),[20,21] in which case, conduction channels near the Fermi level were exclusively ascribed to empty 3d metal orbitals of t_{2g} symmetry.

Conclusion

We present an example of magnetoresistance in a highly conductive single-molecule junction at room temperature composed by supramolecularly trapped metalloporphyrins. The electronic structure of the metal centres plays a crucial role, with only metal-based charge transport pathways in the paramagnetic [Co(DPP)] and [Cu(DPP)] complexes present-

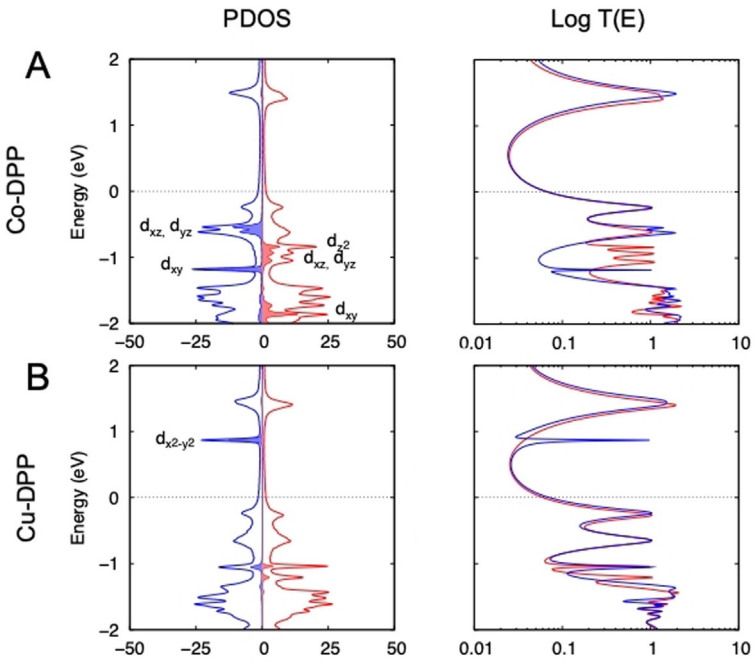

Figure 6. DFT calculated spin-resolved projected density of states (PDOS) and transmission spectra (T(E)) for the conductance feature I of the [Co(DPP)]/PyrMT (A) and [Cu(DPP)]/PyrMT (B) systems obtained with the Siesta and Gollum codes using PBE functional. Filled curves in the PDOS graphs denotes transition metal energy levels. Red and blue colors correspond to the alpha and beta spin contributions, respectively.

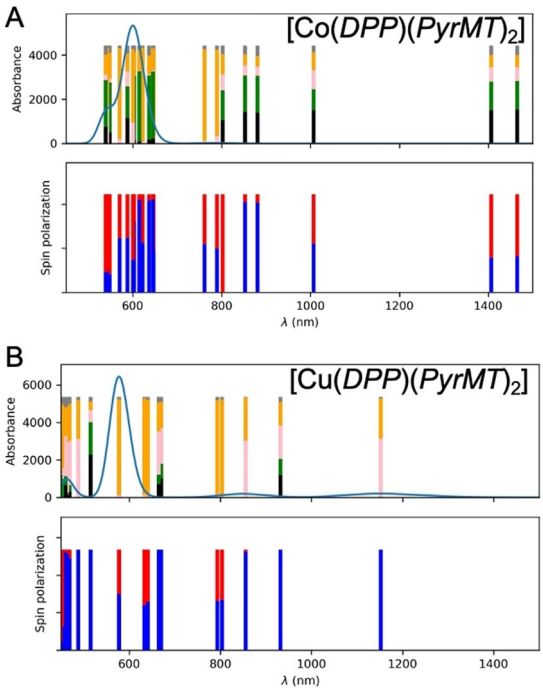

Figure 7. TD-DFT spectrum (TPSSh functional and def2-TZVP basis set) for [Co(DPP)]/PyrMT (A) and [Cu(DPP)]/PyrMT (B). The blue curve corresponds to the calculated spectrum. Each transition is represented in the absorbance graph by a vertical line, where colors indicate their transition composition (metal–metal black, metal–ligand green, ligand–metal pink, ligand–ligand orange). Spin polarization of the transition: red spin up, blue spin down. Results for the four- and five-coordinated models are presented in the Supporting Information section S5.

ing magnetoresistance effect. At the DFT-NEGF level of simulation, the role of the metal d orbital bearing the unpaired electrons is small because the transport, as it is found in the DOS and transmission function calculations, is basically due to the porphyrin orbitals. The magnetic orbitals of the metals play two roles: (i) an indirect role when they mix with the orbitals of the porphyrin responsible of the transport. This effect is too small to justify the observed experimental magnetoresistance; (ii) a direct contribution to the spin-polarized excited states as evidenced in the TDDFT calculations resulting in spin-polarization of the charge transport. This picture is consistent with the experimentally observed modest magnetoresistance values, which is in stark contrast with previously reported $[M(tzpy)_2(NCX)_2]$, (M: Fe or Co; X: S or Se) systems, which present much stronger magnetoresistance effects thanks to the presence of exclusively metal-based spin down polarized orbitals near the Fermi level.[20] Furthermore, the magnetoresistance is strongly dependent on the direction of the tip magnetic polarization evidencing large anisotropy. Perpendicular Ni STM electrode magnetizations to the transport pathways show completely blockage of the transport through the channels with large orbital participation of the metal paramagnetic centers. These experiments demonstrate the crucial role of the electronic structure of the spin-polarized molecular orbitals and their interaction with the electrodes leading to an effective spinterface responsible for the observed magnetoresistance. The use of transition metal complexes opens to a large versatility in device design and to a variety of options concerning the choice of charge carriers' type (their spin, energy, and electron/hole nature) to tune the transport properties in nanoscale molecular spintronic devices.

Acknowledgements

The research reported here was supported by the Spanish Ministerio de Ciencia, e Innovación (grants PGC2018-093863-B-C21, PID2019-108794GB-100 and MDM-2017-0767) and the ERC Grants Fields4CAT (grant 772391) and Tmol4TRANS (grant 724981). I.D.-P. thanks King's College London for start-up funds support. A.C.A. thanks the European Union for a H2020-MSCA-IF-2018 Fellowship (TEChMoDE, 844668). A.M.R. thanks the Ministerio de Ciencia, e Innovación for a predoctoral FPI grant. E.R. thanks Generalitat de Catalunya for an ICREA Academia award and for the SGR2017-1289 grant. N.A.-A. and A.G.-C. thank the Generalitat de Catalunya for the grant 2017SGR1277 and the Severo Ochoa Program for Centers of Excellence in R&D (FUNFUTURE, CEX2019-000917-S). A.G.C. thanks Ministerio de Ciencia e Innovación for Ramon y Cajal grant (RYC-2017-22910). The authors acknowledge the general facilities of the Universitat de Barcelona (CCiT-UB) and the computer

resources, technical expertise and assistance provided by the Barcelona Supercomputing Centre.

Conflict of Interest

The authors declare no conflict of interest.

Keywords: density functional calculations · magnetoresistance · metalloporphyrins · single-molecule junctions · spinterface

[1] S. Sanvito, *Nat. Phys.* **2010**, *6*, 562 – 564.
[2] S. Sanvito, *Chem. Soc. Rev.* **2011**, *40*, 3336 – 3355.
[3] S. Fusil, V. Garcia, A. Barthélémy, M. Bibes, *Annu. Rev. Mater. Res.* **2014**, *44*, 91 – 116.
[4] A. Hirohata, K. Takanashi, *J. Phys. D* **2014**, *47*, 193001.
[5] J. Sinova, S. O. Valenzuela, J. Wunderlich, C. H. Back, T. Jungwirth, *Rev. Mod. Phys.* **2015**, *87*, 1213 – 1260.
[6] S. V. Aradhya, L. Venkataraman, *Nat. Nanotechnol.* **2013**, *8*, 399 – 410.
[7] D. M. Guldi, H. Nishihara, L. Venkataraman, *Chem. Soc. Rev.* **2015**, *44*, 842 – 844.
[8] R. M. Metzger, *J. Mater. Chem.* **2008**, *18*, 4364 – 4396.
[9] D. Xiang, X. Wang, C. Jia, T. Lee, X. Guo, *Chem. Rev.* **2016**, *116*, 4318 – 4440.
[10] A. N. Pal, D. Li, S. Sarkar, S. Chakrabarti, A. Vilan, L. Kronik, A. Smogunov, O. Tal, *Nat. Commun.* **2019**, *10*, 5565.
[11] R. Vincent, S. Klyatskaya, M. Ruben, W. Wernsdorfer, F. Balestro, *Nature* **2012**, *488*, 357 – 360.
[12] J. Schwöbel, Y. Fu, J. Brede, A. Dilullo, G. Hoffmann, S. Klyatskaya, M. Ruben, R. Wiesendanger, *Nat. Commun.* **2012**, *3*, 953.
[13] M. Urdampilleta, S. Klyatskaya, J. P. Cleuziou, M. Ruben, W. Wernsdorfer, *Nat. Mater.* **2011**, *10*, 502 – 506.
[14] S. Wagner, F. Kisslinger, S. Ballmann, F. Schramm, R. Chandrasekar, T. Bodenstein, O. Fuhr, D. Secker, K. Fink, M. Ruben, H. B. Weber, *Nat. Nanotechnol.* **2013**, *8*, 575 – 579.
[15] B. Gohler, V. Hamelbeck, T. Z. Markus, M. Kettner, G. F. Hanne, Z. Vager, R. Naaman, H. Zacharias, *Science* **2011**, *331*, 894 – 897.
[16] R. Naaman, Z. Vager, *Phys. Chem. Chem. Phys.* **2006**, *8*, 2217 – 2224.
[17] R. Naaman, D. H. Waldeck, *Annu. Rev. Phys. Chem.* **2015**, *66*, 263 – 281.
[18] A. C. Aragonès, E. Medina, M. Ferrer-Huerta, N. Gimeno, M. Teixidó, J. L. Palma, N. Tao, J. M. Ugalde, E. Giralt, I. Díez-Pérez, V. Mujica, *Small* **2017**, *13*, 1602519.
[19] R. Naaman, Y. Paltiel, D. H. Waldeck, *J. Phys. Chem. Lett.* **2020**, *11*, 3660 – 3666.
[20] A. C. Aragonès, D. Aravena, J. I. Cerdá, Z. Acís-Castillo, H. Li, J. A. Real, F. Sanz, J. Hihath, E. Ruiz, I. Díez-Pérez, *Nano Lett.* **2016**, *16*, 218 – 226.
[21] A. C. Aragonès, D. Aravena, F. J. Valverde-Muñoz, J. A. Real, F. Sanz, I. Díez-Pérez, E. Ruiz, *J. Am. Chem. Soc.* **2017**, *139*, 5768 – 5778.
[22] J.-J. Li, M.-L. Bai, Z.-B. Chen, X.-S. Zhou, Z. Shi, M. Zhang, S.-Y. Ding, S.-M. Hou, W. Schwarzacher, R. J. Nichols, B.-W. Mao, *J. Am. Chem. Soc.* **2015**, *137*, 5923 – 5929.
[23] F. Djeghloul, F. Ibrahim, M. Cantoni, M. Bowen, L. Joly, S. Boukari, P. Ohresser, F. Bertran, P. Le Fevre, P. Thakur, F. Scheurer, T. Miyamachi, R. Mattana, P. Seneor, A. Jaafar, C. Rinaldi, S. Javaid, J. Arabski, J. P. Kappler, W. Wulfhekel, N. B. Brookes, R. Bertacco, A. Taleb-Ibrahimi, M. Alouani, E. Beaurepaire, W. Weber, *Sci. Rep.* **2013**, *3*, 1272.
[24] M. Galbiati, S. Tatay, C. Barraud, A. V. Dediu, F. Petroff, R. Mattana, P. Seneor, *MRS Bull.* **2014**, *39*, 602 – 607.
[25] A. C. Aragonès, N. Darwish, W. J. Saletra, L. Pérez-García, F. Sanz, J. Puigmartí-Luis, D. B. Amabilino, I. Díez-Pérez, *Nano Lett.* **2014**, *14*, 4751 – 4756.
[26] A. C. Aragonès, N. L. Haworth, N. Darwish, S. Ciampi, N. J. Bloomfield, G. G. Wallace, I. Diez-Perez, M. L. Coote, *Nature* **2016**, *531*, 88 – 91.
[27] B. Xu, N. J. Tao, *Science* **2003**, *301*, 1221 – 1223.
[28] W. Haiss, R. J. Nichols, H. van Zalinge, S. J. Higgins, D. Bethell, D. J. Schiffrin, *Phys. Chem. Chem. Phys.* **2004**, *6*, 4330 – 4337.
[29] A. C. Aragonès, A. Martín-Rodríguez, D. Aravena, J. Puigmartí-Luis, D. B. Amabilino, N. Aliaga-Alcalde, A. González-Campo, E. Ruiz, I. Díez-Pérez, *Angew. Chem. Int. Ed.* **2020**, *59*, 19193 – 19201; *Angew. Chem.* **2020**, *132*, 19355 – 19363.
[30] C. S. Quintans, D. Andrienko, K. F. Domke, D. Aravena, S. Koo, I. Díez-Pérez, A. C. Aragonès, *Appl. Sci.* **2021**, *11*, 3317.
[31] S. Schmaus, A. Bagrets, Y. Nahas, T. K. Yamada, A. Bork, M. Bowen, E. Beaurepaire, F. Evers, W. Wulfhekel, *Nat. Nanotechnol.* **2011**, *6*, 185 – 189.
[32] K. Yang, H. Chen, T. Pope, Y. Hu, L. Liu, D. Wang, L. Tao, W. Xiao, X. Fei, Y.-Y. Zhang, H.-G. Luo, S. Du, T. Xiang, W. A. Hofer, H.-J. Gao, *Nat. Commun.* **2019**, *10*, 3599.
[33] R. R. Holmes, *Prog. Inorg. Chem.* **1984**, *32*, 119 – 235.
[34] A. C. Aragonès, K. F. Domke, *Cell Rep.* **2021**, *2*, 100389.
[35] R. J. Nichols, W. Haiss, S. J. Higgins, E. Leary, S. Martin, D. Bethell, *Phys. Chem. Chem. Phys.* **2010**, *12*, 2801 – 2815.
[36] A. C. Aragonès, N. Darwish, S. Ciampi, F. Sanz, J. J. Gooding, I. Díez-Pérez, *Nat. Commun.* **2017**, *8*, 15056.
[37] C. R. Peiris, Y. B. Vogel, A. P. Le Brun, A. C. Aragonès, M. L. Coote, I. Díez-Pérez, S. Ciampi, N. Darwish, *J. Am. Chem. Soc.* **2019**, *141*, 14788 – 14797.
[38] X. Yao, M. Vonesch, M. Combes, J. Weiss, X. Sun, J.-C. Lacroix, *Nano Lett.* **2021**, *21*, 6540 – 6548.
[39] M. Noori, A. C. Aragonès, G. Di Palma, N. Darwish, S. W. D. Bailey, Q. Al-Galiby, I. Grace, D. B. Amabilino, A. González-Campo, I. Díez-Pérez, C. J. Lambert, *Sci. Rep.* **2016**, *6*, 37352.
[40] *Handbook of Spin Transport and Magnetism*, Chapman and Hall/CRC, London, **2016**.
[41] N. Sobrino, F. Eich, G. Stefanucci, R. D'Agosta, S. Kurth, *Phys. Rev. B* **2021**, *104*, 125115.
[42] J. S. Evans, T. V. Voorhis, *Nano Lett.* **2009**, *9*, 2671 – 2675.
[43] Y. Shu, D. G. Truhlar, *J. Chem. Theory Comput.* **2020**, *16*, 4337 – 4350.

Manuscript received: August 5, 2021
Revised manuscript received: September 23, 2021
Version of record online: November 2, 2021

